

Passive bistatic radar probes of the subsurface on airless bodies using high energy cosmic rays via the Askaryan effect

Remy Prechelt^{1*}, Emily Costello², Rebecca Ghent³, Peter Gorham¹, Paul Lucey², Andrew Romero-Wolf⁴ and Gary Varner¹

¹Department of Physics and Astronomy, University of Hawai'i Mānoa, Correa Road, Honolulu, 96822, Hawai'i, USA.

²Hawai'i Institute of Geophysics and Planetology, University of Hawai'i Mānoa, East-West Road, Honolulu, 96822, Hawai'i, USA.

³Planetary Science Institute, E Fort Lowell Road, Tucson, 85719, Arizona, USA.

⁴Jet Propulsion Laboratory, California Institute of Technology, Oak Grove Drive, Pasadena, 91109, California, USA.

*Corresponding author(s). E-mail(s): prechelt@hawaii.edu;

Abstract

We present a new technique to perform passive bistatic subsurface radar probes on airless planetary bodies. This technique uses the naturally occurring radio impulses generated when high-energy cosmic rays impact the body's surface. As in traditional radar sounding, the downward-beamed radio emission from each *individual* cosmic ray impact will reflect off subsurface dielectric contrasts and propagate back up to the surface to be detected. We refer to this technique as *Askaryan radar* after the fundamental physics process, the Askaryan effect, that produces this radio emission. This technique can be performed from an orbiting satellite, or from a surface lander, but since the radio emission is generated beneath the surface, an Askaryan radar can completely bypass the effects of surface clutter and backscatter typically associated with surface-penetrating radar. We present the background theory of Askaryan subsurface radar and show results from both finite-difference time-domain (FDTD) and Monte Carlo simulations that confirm that

this technique is a promising planetary radar sounding method, producing detectable signals for realistic planetary science applications.

Keywords: Askaryan effect, subsurface radar, cosmic ray, bistatic radar, lunar ice, Cherenkov radiation

1 Introduction

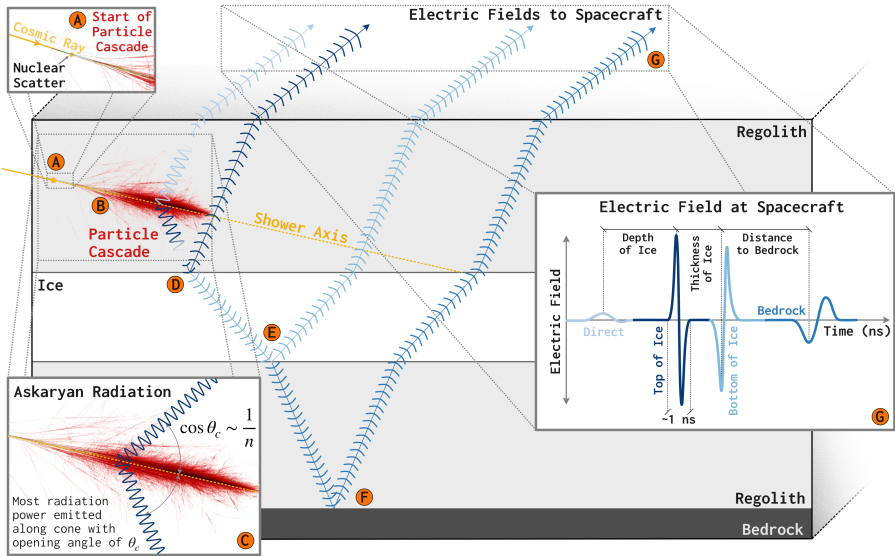
Ground penetrating radar (GPR) has been a powerful and unique tool for performing remote measurements of the subsurface structure and composition of planetary bodies for nearly five decades [1], with previous, current and future targets including the Moon [1, 2, 3, 4], Mars [5, 6, 7], Europa [8], Ganymede [9], and the comet 67P/Churyumov-Gerasimenko [10]. Ground penetrating radar soundings have been performed from the body’s surface, with a lander or rover, and from orbit, with a range of radar frequencies and bandwidths tailored to meet the needs of the particular investigation [11]. The fundamental principle of many of these probes has been the same: an electromagnetic wave is transmitted into the subsurface from the spacecraft and propagates down into the planetary body; the radar “echoes”, reflections from subsurface dielectric contrasts in the volume are observed by a radio receiver and encode information about the composition, structure, and dielectric properties of the subsurface [12, 13].

In this work, we present an innovative new technique for performing completely passive bistatic radar probes of the subsurface on airless or nearly airless planetary bodies using the naturally occurring broadband radio impulses generated when high-energy cosmic rays impact the surface. We refer to this technique as *Askaryan subsurface radar*, named for the fundamental physics process, the Askaryan effect, that generates this impulsive radio emission. This technique can be done from orbit, or from the surface, and has the advantage that the highly-impulsive radar signals are generated *beneath* the surface, completely bypassing the surface clutter and backscatter effects typically associated with orbital radar sounding. This technique has the potential to provide high-horizontal and depth resolution, commensurate with that of a typical lander or rover mission, with the total area coverage of orbital radar sounding instruments, while using only passive radio instrumentation.

Section 1.1 finishes the introduction to this technique, and Section 2 presents the background theory and simulation methodology that we use to validate this concept, including a discussion of the cosmic ray flux in Section 2.1.1, the theory of high energy particle cascades in dense media in Section 2.1.2, and the origin of the radio impulses via the Askaryan effect in Section 2.1.4. Section 3 presents the results of a pair of simulations of this technique using both finite-difference time-domain (FDTD) and Monte Carlo (MC) techniques

in Section 3.1 and Section 3.2, respectively, and discusses an immediate application of this technique to the detection of water ice in the permanently shadowed regions at the lunar poles.

1.1 Askaryan Subsurface Radar



Askaryan Subsurface Radar

Distances and angles not necessarily to scale

Fig. 1: A diagram illustrating the new *Askaryan subsurface radar* technique proposed in this work, for an example application of detecting a coherent ice layer buried in regolith. Each orange marker has a corresponding description in the text of Section 1.1.

A diagram demonstrating the key features of the *Askaryan radar* technique is shown in Figure 1, for an example application of detecting a buried ice layer in the lunar regolith as might potentially exist in the permanently shadowed regions at the lunar poles [14]. We introduce the core concepts of this technique, starting with the initial cosmic ray impact and ending with the detection of the radio emission by a radar receiver; each orange marker in the text corresponds to an identical marker in Figure 1.

- (A)** Planetary bodies in the solar system that lack a dense atmosphere are continually bombarded by both solar, galactic, and (likely) extra-galactic cosmic rays. When these cosmic rays impact the surface, they almost immediately initiate a high energy particle cascade.
- (B)** This particle cascade, starting with the nuclei from the initial collision with the cosmic ray which goes on to collide with other nuclei (and so on), develops in length and particle number until it potentially contains

billions of charged particles (depending upon the cosmic ray energy). In high energy physics, these particle cascades are known as "showers" and have been a mainstay of particle physics for nearly a century [15].

- Ⓒ These high energy particle cascades emit 100% linearly polarized wide-bandwidth coherent radio impulses as they develop in the subsurface; this emission process is known as the Askaryan effect. The source of this emission is the coherent radio Cherenkov radiation from the 20%-25% compact negative charge excess that forms along the front of all high energy particle cascades in dense media.
- Ⓓ Ⓔ Ⓕ The Askaryan emission from the cascade propagates down into the subsurface, with unique reflections generated by each dielectric contrast in the volume (in this example, the regolith-ice, ice-regolith, and regolith-bedrock interfaces) just as in traditional radar sounding.
- Ⓖ An example of the signals that might be observed by a spacecraft for the subsurface strata of Figure 1, in addition to the direct signal observed *without* reflection, is shown in inset Ⓖ and encode valuable information about the structure and composition of the subsurface.

This technique has been previously performed *on Earth* with the Antarctic Impulsive Transient Antenna (ANITA). ANITA, a long-duration balloon-borne cosmic ray and neutrino observatory, has detected $\mathcal{O}(60)$ ultrahigh energy cosmic rays via their impulsive radio emission after it was *reflected off* the Antarctic surface (a completely analogous process to the detection of lunar ice described above) [16]. While these detections are not scientifically interesting on Earth due to existing high resolution measurements of both the cosmic ray flux [17], and the Antarctic surface from airborne and orbital radar instruments [18], they do provide important validation of, and heritage to, this technique. Therefore, the question posed by this work is as follows: is the detection rate and sensitivity of an Askaryan radar mission scientifically compelling for use in planetary science applications?

2 Background theory & simulation methods

The underlying physics of cosmic ray-induced cascades, and their associated radio emission via the Askaryan effect, is extremely well studied with extensive terrestrial measurements by dozens of observatories over the last century [15]. In the following sections, we present a summary of the theory of particle cascades as it relates to our concept and discuss the data and models needed to perform accurate simulations of this technique.

2.1 Background theory

In the following sections, we present the background theory of this technique, including the high energy cosmic ray flux, the physics of particle cascades, and the generation of the radio emission via the Askaryan effect.

2.1.1 Flux of high energy cosmic rays

The flux of high energy cosmic rays is a power-law-like flux, $E^{\gamma(E)}$, with exponent, $\gamma(E)$, varying from -2.7 to -3.3, in the energy range applicable to this technique. The Askaryan radar technique is currently most amenable to cosmic rays with energies above roughly 10 PeV (10^{16} eV) due to thermal noise constraints on the radio detection, and extending up to the highest observed cosmic rays, so-called ultrahigh-energy cosmic rays (UHECRs), at ~ 500 EeV (5×10^{20} eV). The flux of high energy and ultrahigh energy cosmic rays over this energy range is shown in Figure 2. Above 100 PeV, approximately $\sim 4 \times 10^4$ cosmic rays impact every square kilometer of a planetary body per year, but due to the steeply falling cosmic ray flux spectrum ($\propto E^{\approx -3}$), lower energy cosmic rays are the dominant contributor to the overall detection rate given a fixed cosmic ray energy threshold. Due to their propagation through galactic and extra-galactic fields, the arrival direction of high energy cosmic rays, which can likely propagate from sources at distances up to $\mathcal{O}(100 \text{ Mpc})$, are highly isotropic with respect to the surface of any airless body in the solar system and can be assumed to arrive (stochastically) uniformly in time and in solid angle.

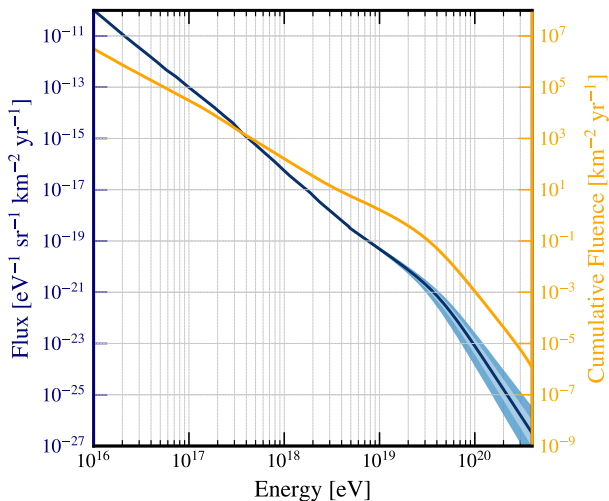


Fig. 2: The all-particle flux of high energy and ultrahigh energy cosmic rays measured by the Pierre Auger observatory from 10 PeV to 500 EeV is shown in blue (left axis) along with the 1σ (light blue) and 2σ (dark blue) uncertainty region for the measurement, which starts to become significant above 5 EeV. The inverse cumulative fluence, the total fluence of particles *above* a given energy ($\text{km}^{-2} \text{yr}^{-1}$), is shown in orange (right axis) [19].

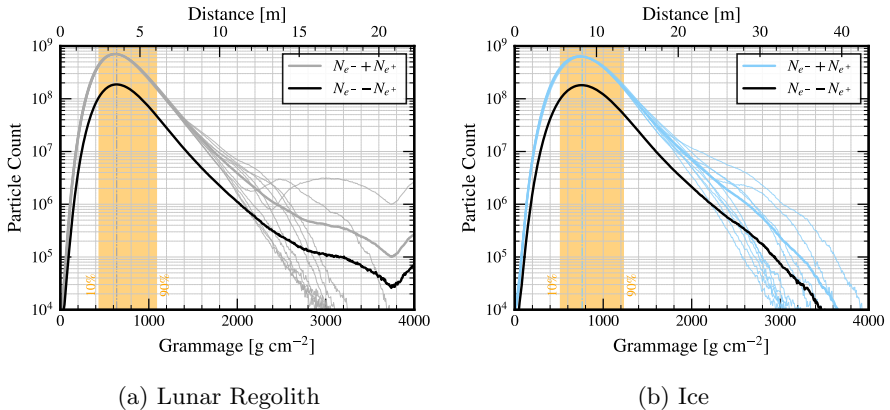


Fig. 3: The longitudinal profile of the total electronic charge (electrons *and* positrons in grey or blue), and the profile of the negative charge excess (electrons *minus* positrons in black) for a sample of 1 EeV proton-initiated cascades in lunar regolith and in ice. The thick grey (blue) and black lines indicate the average profile over ten showers for regolith (ice), while the thin lines show the individual profiles from each simulated shower. The orange band indicates the 10% to 90% cumulative charge length for the average profiles and represents the “bulk” of the shower development. The particle cascades were simulated with the TIERRAS code [20], a modification of the ZHAireS code for use in dense media [21]. For all simulations, lunar regolith is simulated with a nominal density of $\rho = 1.8 \text{ g cm}^{-3}$ and refractive index $n = 1.78$, and ice is simulated with $\rho = 0.924 \text{ g cm}^{-3}$ and $n = 1.305$

2.1.2 Cosmic ray cascades in dense media

When primary high energy cosmic rays impact the dense surface of a nearly airless planetary body, they initiate particle cascades via high energy inelastic collisions with nuclei in the medium. These cascades develop predominantly along the original direction of the cosmic ray (known as the *shower axis*—see Figure 1) and grow in size until they reach a maximum number of particles, at which point energy losses to the medium continually slows the production of new particles until the shower development stops (as existing particles in the cascade no longer have sufficient mass-energy to produce new particles in the shower). The longitudinal profiles, the number of particles in the cascade projected onto the shower axis, of a population of 1 EeV proton-initiated cosmic ray cascades in the lunar regolith and in ice is shown in Figure 3a and Figure 3b, respectively.

The development of a high energy cascade is driven by the energy of the cosmic ray primary and the total grammage (density multiplied by length, measured in g cm^{-2}) experienced by the shower as it develops. The grammage, usually denominated as X , where the number of particles in the shower

is at a maximum is known as *shower maximum*, and is denoted as X_{\max} . As medium density decreases, the average length of these showers increases; showers in regolith-like materials are typically $\mathcal{O}(10\text{ m})$ long, with X_{\max} occurring at $\sim 4\text{ m}$, whereas showers in ice or air can be tens or thousands of meters in length, respectively. However, when expressed in terms of grammage (top axis of Figure 3a and Figure 3b), showers in different media are highly comparable with shower maximum typically occurring at 600 g cm^{-2} to 800 g cm^{-2} at 1 EeV with X_{\max} increasing as the primary particle energy increases.

2.1.3 Development of a negative charge excess in high energy cascades

These particle cascades develop a 20%-25% negative charge excess as they develop, as atomic electrons are preferentially upscattered into the shower and positrons (produced via pair production in the cascade) are annihilated against this same population of atomic electrons. Therefore, high energy particle cascades are not electrically neutral and this negative charge excess is typically centimeters thick and millimeters-wide in dense media like regolith and is concentrated along the front of the cascade [22]. The longitudinal profile of negative charge excess of the a population of 1 EeV proton showers is shown in the solid black lines of Figure 3a and Figure 3b.

2.1.4 Askaryan Effect

All charged particles moving faster than the phase speed of light in a medium (c/n) emit broadband Cherenkov radiation that is typically observed in the optical and near-ultraviolet wavelengths (due to the Cherenkov power spectrum increasing with frequency) [23, 24, 15]. When observed at wavelengths larger than the physical size of this compact charge excess, typically a few MHz to a few GHz depending upon the medium, the radio-wavelength Cherenkov radiation from each particle in the cascade is observed *coherently* and the entire charge excess is observed as a relativistic particle emitting coherent radio Cherenkov emission [25]. The coherent radio and microwave emission from the negative charge excess in a high energy shower is known as the *Askaryan effect* and has been experimentally measured in a variety of media over more than two decades [25, 26, 27, 28], and forms the basis for a multiple existing cosmic ray and neutrino observatories on Earth [29, 30, 31].

The electric field created by the Askaryan effect is 100% linearly polarized, with a polarization vector that is uniquely determined by the cosmic ray trajectory and observation direction, and the emitted electric fields are extremely impulsive with typical durations of $\mathcal{O}(1\text{ ns})$ close to the angle of peak emitted power (the Cherenkov angle) [32]. The wide bandwidth and high linear polarization of the emission from the Askaryan effect makes it a strong potential candidate for use in surface penetrating radar.

The total radio-frequency power emitted via the Askaryan effect scales quadratically with the energy of the incident cosmic ray, so an experiment

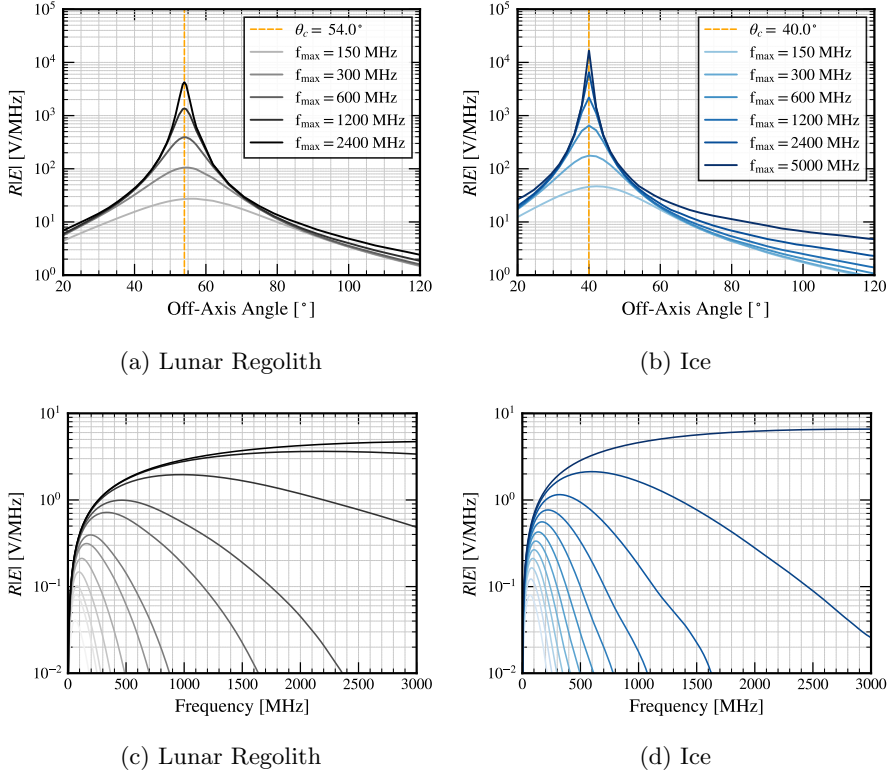



Fig. 4: *Top:* The angular spectrum of the electric potential spectral density for various upper frequency limits on the Askaryan spectrum. The vertical orange line indicates the location of the Cherenkov angle in the particular simulation configuration. *Bottom:* The average electric potential spectral density at various off-axis angles for the same cascades in regolith and ice, respectively. Near the Cherenkov angle, the Askaryan spectrum extends well above 3 GHz in both media when observed at the Cherenkov angle. For all simulations, lunar regolith is simulated with a nominal density of $\rho = 1.8 \text{ g cm}^{-3}$ and refractive index $n = 1.78$, and ice is simulated with $\rho = 0.924 \text{ g cm}^{-3}$ and $n = 1.305$

sensitive to three orders of magnitude of cosmic ray energy (i.e. 0.5 EeV to 500 EeV) will observe six orders of magnitude in radio power. This power is emitted with a conical beam pattern aligned with the shower axis (i.e. uniformly in azimuth around the shower axis but narrowly beamed in polar "off-axis" angle). The average angular spectrum of the electric potential for the same population of proton-initiated cascades in regolith and ice is shown in Figure 4a and Figure 4b. The polar opening angle of this conical beam is determined by the Cherenkov angle and is given by $\cos\theta \sim 1/n$, where n is the refractive index of the medium (inset  in Figure 1), with a beamwidth

(“thickness” of the conical beam) that depends on frequency but is nominally a few degrees for wide bandwidths.

The Askaryan frequency spectrum shows the same characteristic linear rise over frequency as the underlying Cherenkov emission; this linear rise continues down to wavelengths such that the cascade is no longer observed coherently by an observer (when the size of the charge excess becomes comparable to wavelength). This turnover frequency is dependent upon the angle between the observation direction and the shower axis (the “off-axis” angle). The average frequency spectra of the same population of cascades in regolith and ice is shown in Figure 4c and Figure 4d, respectively. When observed close to the Cherenkov angle, where the coherence is maximized, Askaryan radiation can be extremely broadband, extending to $\gtrsim 4$ GHz in both ice and regolith; as the observer moves further *off-cone* (i.e. away from the Cherenkov angle), the cascade is no longer observed coherently and the upper limit of the spectral density decreases.

2.2 Simulation Methods

We analyze our Askaryan radar concept using two different simulation methods: (a) a finite-difference time-domain (FDTD) simulation that is highly accurate, capturing the full-wave electromagnetic behavior of the Askaryan emission process and subsurface reflection, but is computationally intractable for use in a comprehensive study of this technique; and, (b) a semi-analytical Monte Carlo (MC) simulation that is orders of magnitude faster, at the cost of lower fidelity, and is therefore computationally tractable for exploring the available phase space.

We perform these simulations for the simplified geometry of Figure 1—a subsurface layer of ice buried within an otherwise uniform volume of regolith—but we vary the depth, thickness, roughness, and composition of the buried layer to probe the phase space of subsurface structure and composition detectable by an Askaryan radar for this application. This example geometry is motivated by the search for subsurface water ice on the Moon that may have been buried by hydrated impacts and preserved under several meters of regolith in the permanently shadowed regions at the lunar poles for geologic time [14].

2.2.1 Finite-Difference Time-Domain Simulations

The finite-difference time-domain (FDTD) algorithm is a technique for performing high-fidelity computational electrodynamics simulation for arbitrary geometries and sources. The FDTD method discretizes Maxwell’s equations on a spatio-temporal grid and directly evolves the electric and magnetic field components in each grid cell over time enabling accurate simulations of the generation of Askaryan emission from a relativistic shower, and the subsequent reflection off realistic subsurface layers [33]. While highly accurate, FDTD simulations are extremely computationally expensive and are therefore limited

to relatively small simulation domains without becoming intractable. In our work, we simulate the volume of the subsurface reflector over several Fresnel zones, thus typically $50 \times 10 \times 15 \text{ m}^3$ (length by width by depth), and an additional volume above the surface, $50 \times 10 \times 20 \text{ m}^3$ (length by width by height) to ensure that radiation has transitioned to the Fraunhofer zone where we can propagate the fields, using analytical transforms, to the electric field detected by the spacecraft in the far field.

As there is no currently available FDTD code that can directly simulate the evolution of high energy cosmic ray induced particle cascades, we first simulate proton-initiated cascades in the lunar regolith using TIERRAS [20]—a well-validated code for the simulation of cascades in dense media—and use the longitudinal profile of the charge excess (Figure 3a and Figure 3b) to construct an equivalent relativistic time-varying current source in the commercial XFDTD software that reproduces the simulated charge excess profiles. We use the commercial FDTD software XFDTD to perform each simulation [34]. The Askaryan radiation is automatically generated by the discretized form of Maxwell’s equations from the inserted current profile, propagates down into the subsurface, and reflects off a rough surface based on the Change-3 Yutu rover data for a 60 m long track, which implies an RMS height deviation of about 0.5 m over the 60 m range [35, 36]. To translate this measurement to the $\sim 2 \text{ m}$ typical diameter of the Fresnel zone for the Askaryan pulse reflection, we simulate a 50 m diameter 2D self-affine (eg. fractal) surface [37] with characteristics based on the measured rover track RMS and power spectral density, and then sample the sub-region RMS over patches with the average size of the Fresnel zone, with a plane-slope removed.

2.2.2 Monte Carlo Simulation Method

As this technique relies on cosmic ray impacts that occur stochastically over time, area, and solid angle, an Askaryan radar instrument must continually observe a given surface waiting for a cosmic ray impact to illuminate the subsurface layer from an unknown direction. The rate of subsurface radar detections (referred to as “*events*” in the following text) made by an Askaryan radar depends on the cosmic ray flux, the physical properties of the subsurface, the geometry of the observation, and the sensitivity of the spacecraft. Given a distribution of subsurface reflectors embedded in a subsurface volume, the *average* detection rate, $d\bar{N}/dt$, can be approximately expressed as:

$$\begin{aligned}
 \frac{d\bar{N}}{dt} = & \underbrace{\int_{E_{\min}}^{10^{21} \text{ eV}} dE \mathcal{F}(E)}_{\text{Cosmic ray flux}} \underbrace{\int_{\Sigma} d\vec{\sigma} \int_{\Omega} d\vec{\omega}}_{\text{Geometric acceptance}} \\
 & \underbrace{\int_0^{R_{\text{moon}}} dz \int_0^{\infty} d\Delta n \tilde{P}(z, \Delta n)}_{\text{Depth distribution of reflectors}} \\
 & \underbrace{\int dX \tilde{P}(\vec{X}_{\max} | E, \vec{\omega}, \vec{\sigma})}_{\text{Location of } \vec{X}_{\max}} \\
 & \underbrace{\int_{\mathcal{E}_{\min}}^{\infty} d\mathcal{E}_f \tilde{P}(\mathcal{E}_f | E, \vec{\sigma}, \vec{\omega}, \vec{x}(t), \vec{X}_{\max}, \Delta n, z)}_{\text{Reflected Askaryan radiation at spacecraft}}
 \end{aligned} \tag{1}$$

where,

- \bar{N} = the *average* number of subsurface radar detections (events) made by the spacecraft,
- $d\vec{\sigma}$ = an element of differential area on the planetary body,
- Σ = the total area of the body visible from the spacecraft at time t ,
- $d\vec{\omega}$ = an element of differential solid angle centered at $d\vec{\sigma}$,
- Ω = the total solid angle of the cosmic ray flux visible from $d\vec{\sigma}$,
- E = the energy of the incident cosmic ray,
- E_{\min} = the minimum cosmic ray energy the spacecraft is able to detect; this depends directly on \mathcal{E}_{\min} ,
- $\mathcal{F}(E)$ = the incident isotropic cosmic ray flux ($\text{km}^{-2} \text{s}^{-1} \text{sr}^{-1} \text{eV}^{-1}$),
- z = depth below the surface of the moon,
- Δn = the dielectric contrast between two subsequent differential depths,
- $\tilde{P}(z, \Delta n)$ = the probability density of finding a dielectric contrast Δn at a depth z ,
- X = the grammage experienced by the cosmic ray shower as it develops along the shower axis,
- $\tilde{P}(\vec{X}_{\max} | \dots)$ = the probability density of shower maximum occurring at a grammage \vec{X}_{\max} given the parameters of the cosmic ray,
- \mathcal{E}_f = the electric field from the subsurface reflector *at the spacecraft*,
- \mathcal{E}_{\min} = the *minimum* electric field *detectable by the spacecraft*,
- $\tilde{P}(\mathcal{E}_f | \dots)$ = the probability density of observing an electric field of \mathcal{E}_f *at the spacecraft* given the parameters of the event.

The complexity of propagating the Askaryan emission from the shower, to each subsurface layer, and back up to spacecraft to be detected is included in the function $\tilde{P}(\mathcal{E}_f|\dots)$.

While the FDTD method provides the highest fidelity for *individual* cosmic ray impacts, it is computationally intractable to use FDTD simulations to evaluate $\tilde{P}(\mathcal{E}_f|\dots)$ in the high-dimensional integral of Equation 1. Therefore, to evaluate Equation 1, we use semi-analytical models in a Monte Carlo (MC) integration scheme. This is many orders of magnitude faster than performing full FDTD simulations for each individual cosmic ray impact and allows for a study of the phase space of subsurface structures and compositions that could be detected by an Askaryan radar instrument.

The methodology for a single Monte Carlo trial, used to evaluate Equation 1, is as follows:

1. We start by choosing an impact point uniformly on the surface of the planetary body within view of the spacecraft and choose a cosmic ray direction uniformly in solid angle.
2. We sample a grammage for shower maximum from the measured distribution of $\langle X_{\max} \rangle$ and $\langle \sigma_{X_{\max}} \rangle$ (the fluctuation in X_{\max} on a shower-by-shower basis) as a function of cosmic ray energy as measured by the Pierre Auger Observatory [38].
3. We then use a pre-calculated library of cosmic-ray regolith cascades simulated using the TIERRAS code to estimate the longitudinal charge profile of the shower along the shower axis [20].
4. For each allowable propagation path between X_{\max} and the observer (spacecraft), we use the semi-analytical method of Reference [32] to calculate the electric field waveform that is emitted in the direction of the observer (along both the direct and reflected propagation paths to the spacecraft).
5. We propagate these emitted electric fields down to each subsurface layer, apply the appropriate reflection coefficients, propagate them back up to the surface, and refract each signal out to the spacecraft (using a geometrical optics propagation model), including the Fresnel coefficients at all relevant surface and subsurface boundaries, the attenuation due to propagation in regolith, and the divergence due to the near field refraction at the surface (as the particle cascade acts as a near-field line source with respect to the surface refraction point).
6. The direct and reflected electric fields at the spacecraft are then compared with a spacecraft instrument model to determine whether this specific Monte Carlo trial would have triggered the observatory and been detected.

Finally, the collected sample of Monte Carlo trials are weighted by the cosmic ray flux to calculate the rate of detected events. For this simulation, we directly evaluate the differential flux of ultrahigh energy cosmic rays, $d^4N/(dE dA d\Omega dt)$, as measured by the Pierre Auger Observatory [38].

For the specific lunar simulation of Figure 1, we model the lunar regolith as a uniform volume with density 1.8 g cm^{-3} , uniform radio refractive index of

1.78, and a radio loss tangent of 6.5×10^{-4} in the cold permanently shadowed regions at the lunar poles. The subsurface ice is simulated with varying thicknesses, depths, and purities with 100% pure ice assumed to have a density of 0.924 g cm^{-3} and a refractive index of 1.305 (chosen to be consistent with the ice deposition models of [14]); other purities are modeled as a combination of regolith and ice with properties calculated via a composition-fraction weighted sum of the logarithm of the refractive indices of ice and regolith, respectively.

3 Results

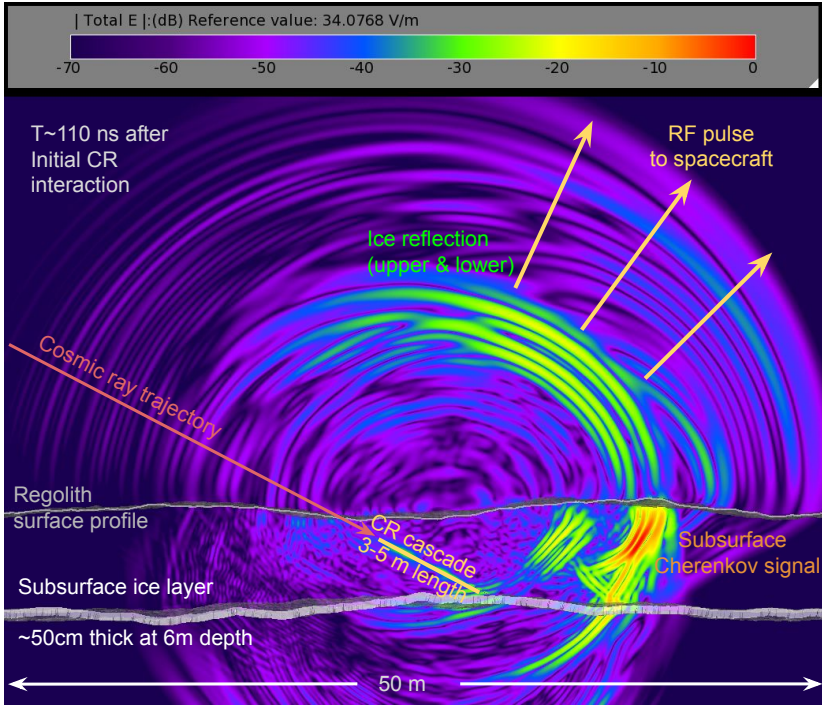
In this section, we present the results of our finite-difference time-domain and Monte Carlo studies of the Askaryan radar technique in the example application of searching for buried ice at the lunar poles.

3.1 Finite-Difference Time-Domain Results

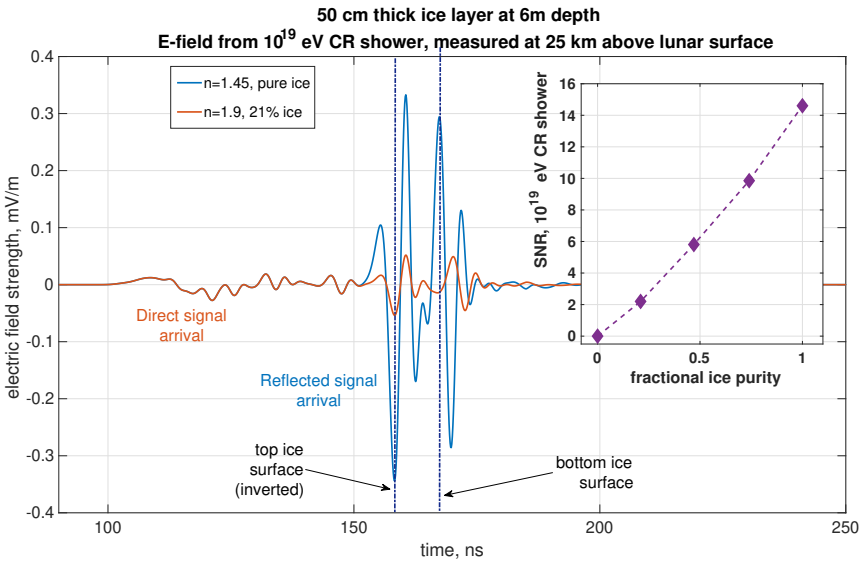
An annotated time snapshot of the direct and reflected electric fields from a cosmic ray induced cascade in the lunar regolith with a 50 cm thick ice layer 6 m below the surface is shown in Figure 5a; the corresponding time-domain electric field waveform observed at a spacecraft orbiting 25 km above the surface is shown in Figure 5b.

The first wavefronts (furthest to the upper right in blue and light purple) are the *direct* emission from the cascade, observed without reflection, and are the first waveforms to arrive at the spacecraft. As shown in Figure 4a and Figure 4b, as the observation direction moves further off-cone the emitted power and total bandwidth decreases, so the direct pulse observed at the spacecraft is typically weaker and less impulsive than the more on-cone reflected pulses (although, the direct pulses do not suffer from the attenuation due to the longer path through the regolith of the reflected wavefronts or the subsurface Fresnel reflection coefficient). This can be seen in the small amplitude and broad pulse width of the direct (orange) waveform in Figure 5b. For events for which the direct emission is identifiable, the relative timing between the direct and reflected impulses provides a powerful fiducial for the depth of each subsurface layer.

Since Askaryan radiation is strongly beamed around the Cherenkov angle ($\sim 30^\circ - 60^\circ$ off the cosmic ray axis depending upon the material— $\sim 54^\circ$ in the lunar regolith), the reflected waveforms, seen as two bright green wavefronts in Figure 5a, are significantly stronger and are highly impulsive. Even when including a rough ice surface for the reflection, the corresponding pulse widths are only a few nanoseconds in duration. In the geometry of this simulation, the regolith-ice and ice-regolith reflections have inverted polarity with respect to each other due to the change in sign of the Fresnel reflection coefficient. This clear polarity inversion allows for distinguishing the pulses from the top and bottom of any subsurface ice layer, and also acts as a direct probe of the thickness of the subsurface reflector.



(a)



(b)

Fig. 5: *a)* A vertical slice of the electric field magnitude from a 3D FDTD simulation of the Askaryan emission from a cosmic ray-induced cascade in the lunar regolith, with a rough ice layer buried below the surface. *b)* The time-domain electric field measured at a spacecraft 25 km above the lunar surface from a similar simulation as *a)*. The electric field is shown for pure ice (blue) and extremely impure ice (orange).

The inset in Figure 5b shows the signal to noise ratio achieved by this 10 EeV cosmic ray as a function of the ice purity or equivalently, the refractive index of the layer compared to the regolith. In this case, at an orbital altitude of 25 km, an Askaryan radar could achieve an electric field signal to noise ratio (SNR) greater than two for ice purities down to $\sim 20\%$ (i.e. 80% regolith by weight), allowing this technique to explore a range of subsurface compositions.

Due to the computational cost of FDTD simulations, we are only able to run a small number of discrete geometries, but they confirm the validity of the fundamental principles of this technique.

3.2 Monte Carlo Results

The results from our Monte Carlo calculation of the subsurface detection rate (Equation 1) for various subsurface and instrumental parameters are shown in Figure 6. Since there is no active transmitter in an Askaryan radar, the overall event rate is set by the combination of the sensitivity of the spacecraft, the geometry of the detection, the (fixed) cosmic ray flux, and the (fixed) properties of the subsurface (i.e. attenuation length, dielectric contrast with the volume, etc.). Therefore, the geometry and spacecraft sensitivity are the two design parameters available for increasing the rate of subsurface detections given a fixed subsurface composition, thus these are the primary parameters that we vary in our studies.

3.2.1 Detectability of Askaryan Radar Signals

Since the radio emission detected by an Askaryan radar can come from anywhere within the field of view of the spacecraft, at any time, with electric fields extending orders of magnitude above and below the threshold of the instrument, an Askaryan radar instrument must be able to continuously trigger on oncoming radio signals that may *potentially* be an Askaryan subsurface signal, and localize the received radar emission back to a subsurface location. This “trigger threshold” is typically set so that the lowest signal-to-noise ratio (SNR) subsurface reflections that could potentially be identified in an offline analysis are captured.

This can be accomplished with a multi-channel beamforming radar receiver whose signals can be coherently combined in real-time to create highly-directional synthetic *beams* that can be used to reconstruct the subsurface location of the received signal, even when the single-antenna signal-to-noise ratio (SNR) is low. An interferometric or multi-channel instrument design has extensive heritage in the field of cosmic ray and neutrino astrophysics, where it has been used by a host of existing Askaryan detection experiments [29, 30, 31, 39]. In particular, this was the technique used by the ANITA instrument to identify its sample of ice-reflected cosmic rays during its circumpolar orbit of Antarctica, with $\sim 0.1^\circ$ resolution on the incoming radio direction, exactly as would be performed on a potential future Askaryan radar mission [16].

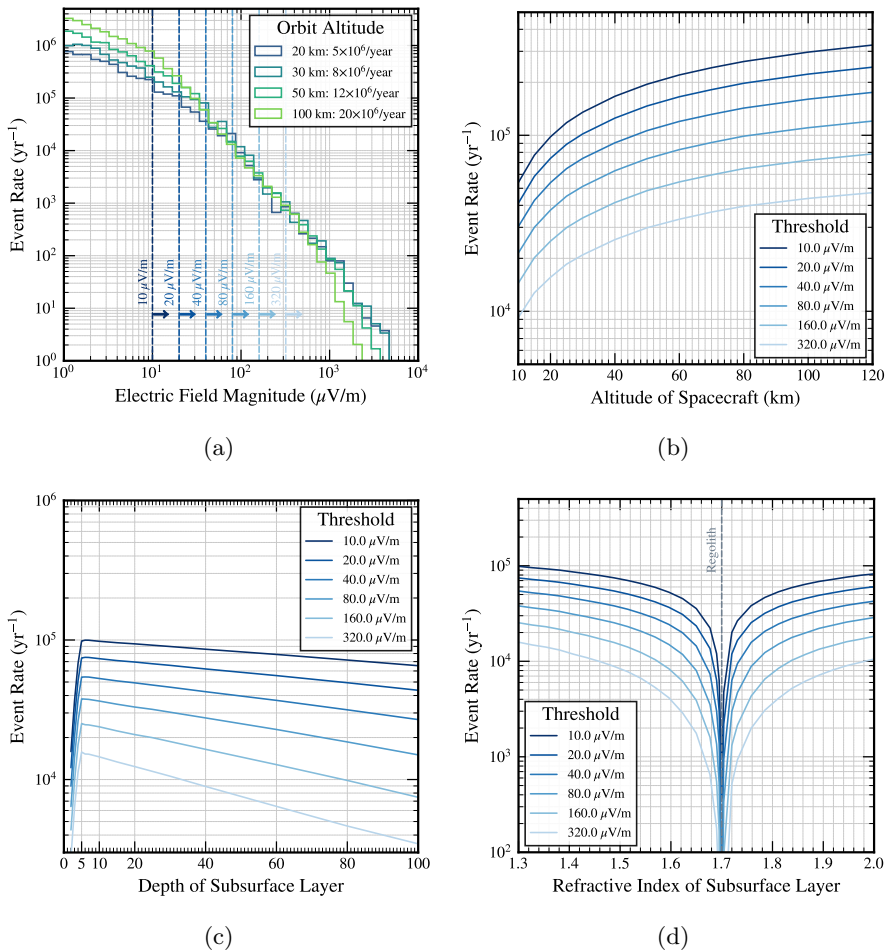


Fig. 6: *a)*: The distribution of Askaryan electric field at the spacecraft from a uniform ice layer buried 5 m below the lunar surface for various spacecraft orbital altitudes. The blue dashed vertical lines show the location of the trigger thresholds used in the other figures. *b)*: The detected event (yr^{-1}) as a function of spacecraft altitude for various detection thresholds. *c)*: The detected event (yr^{-1}) as a function of the depth of the subsurface layer for various detection thresholds; these simulations include a radio attenuation length for the regolith which is responsible for the decline in event rate for deeper layers (see text). *d)*: The detected event (yr^{-1}) as a function of the refractive index of the subsurface layer; the index of the regolith, where no dielectric contrast would be observed, is denoted by the vertical gray dashed line.

3.2.2 Maximum Subsurface Detection Rate

There is a practically unlimited number of cosmic ray impacts on the surface of airless bodies: $\gtrsim 35,000$ per km^2 per year above 100 PeV and $\gtrsim 10^9$ per km^2 per year above 1 PeV, so the detection rate is effectively determined by the minimum cosmic ray energy detectable by the spacecraft (which is, in turn, determined by the electric field threshold of the instrument) assuming there are subsurface reflectors present. Figure 6a shows the simulated distribution of integrated electric field at the spacecraft from cosmic rays with energies between 500 PeV and 500 EeV, for different (circular) orbital altitudes of the spacecraft above the surface of the Moon. This energy span is chosen as a realistic range that could plausibly be detected by a small orbital Askaryan radar mission. Since the galactic cosmic ray flux extends for $\gtrsim 9$ orders of magnitude below this threshold, a larger, more sensitive, mission could detect significantly more detections than presented here, with the detection rate growing rapidly with decreasing threshold.

For each of these initial simulations, we assumed a nominal 1 m thick ice layer with a refractive index of 1.305 buried 5 m below the surface of the regolith. Due to the falling cosmic ray energy spectrum, the electric field spectrum is also decreasing (since the emitted Askaryan electric field strength scales linearly with cosmic ray energy). The legend counts the total number of observed electric fields (at the spacecraft) with total magnitude greater than $1 \mu\text{V}/\text{m}$ when integrated over the frequency range between 50 MHz and 1 GHz. For the simulated lunar orbits, the total number of subsurface reflections observed at the spacecraft exceeds 10^6 in all cases, extending up to 2×10^7 for a 100 km lunar orbit. Figure 6a also shows the six different electric field thresholds, from $10 \mu\text{V}/\text{m}$ to $320 \mu\text{V}/\text{m}$, that are used in the *other* plots in Figure 6 to demonstrate the realized (detected) event rate for a spacecraft with the given electric field sensitivity. The range of electric field thresholds were chosen to cover a range of possible sensitivities that might be achievable with a lunar orbiting Askaryan radar mission with a small beamformed antenna array.

The scaling of the total event rate as a function of orbit altitude is shown in Figure 6b. A lower orbit restricts the total geometric surface area viewable from the spacecraft (which reduces the total event rate as cosmic rays impact uniformly in area), but the reduced cosmic ray to spacecraft distance allows a greater fraction of any reflections to be detected given a fixed spacecraft sensitivity.

Alternatively, a higher orbit, with corresponding larger surface area coverage, will view more cosmic ray impacts but with an attenuated electric field strength, reducing the detection efficiency. As shown in Figure 6b, an Askaryan radar is broadly sensitive over a wide range of orbital altitudes, from 10 km (a potentially unstable orbit for the Moon) up to in excess of 120 km, and can be optimized for a specific application or performance (i.e. resolution on the ground, requiring lower altitudes, or maximizing the number of events that would require higher altitudes).

3.2.3 Maximum Subsurface Detection Depth

Unlike most other radar techniques, Askaryan subsurface radar does not have a fixed depth limit but instead has a decreasing detection rate as the depth of the subsurface reflector increases. This is shown in Figure 6c. As discussed in Section 2.1.4, the power emitted via the Askaryan effect scales quadratically with the primary energy of the cosmic ray, so the emitted power will vary by ~ 6 orders of magnitude for an instrument sensitive to cosmic rays between 0.5 EeV and 500 EeV. For near surface reflectors, the total radio path length through the regolith is at a minimum, so the majority of cosmic rays above the minimum energy are potentially detectable and the event rate is maximized. As the subsurface layer under consideration moves deeper, the regolith path length increases and a higher energy cosmic ray is required in order to exceed the electric field threshold. Since the cosmic ray energy spectrum is steeply falling, the higher energy cosmic rays that are needed to probe progressively deeper reflectors are progressively more rare, decreasing the detection rate, but still allowing for the detection of ice layers down to depths in excess of $\mathcal{O}(100\text{ m})$ with these rarer ultrahigh energy cosmic ray.

For very shallow reflectors ($\lesssim 3\text{ m}$), the cosmic ray induced cascades have not completely developed and therefore emit less Askaryan power (as there is an underdeveloped charge excess in the cascade). However, the *total* charge in the shower will emit coherent transition radiation as it cross into, and out of, the subsurface layer that could also potentially be detected by an Askaryan radar instrument, improving its sensitivity to very shallow reflectors; the detection and reconstruction of this coherent radio transition radiation, and its use as a near-surface radar, will be explored in a later work.

4 Conclusion

We have demonstrated preliminary simulations of a new passive radar sounding technique, *Askaryan subsurface radar*, that has the potential to be a promising new method for performing subsurface radar probes on airless or nearly airless planetary bodies. One of the prime advantages of the Askaryan radar technique is that the radio emission is generated beneath the surface, completely bypassing the effects of surface clutter and dispersion that adversely affects traditional orbital radar sounding. Our detailed FDTD and Monte Carlo simulations demonstrate that this technique would allow a small surface or orbital antenna array to detect buried subsurface ice layers in the regolith over the vast majority of the phase space predicted by current models, without any active radar instrumentation. This technique can be applied to *any* subsurface body without a dense atmosphere, including icy satellites (such as Ganymede), and further work will adapt and improve these simulations for other surface penetrating planetary science applications.

References

- [1] Porcello, L.J., Jordan, R.L., Zelenka, J.S., Adams, G.F., Phillips, R.J., Brown, J. W. E., Ward, S.H., Jackson, P.L.: The Apollo lunar sounder radar system. *IEEE Proceedings* **62**, 769–783 (1974)
- [2] Ono, T., Oya, H.: Lunar radar sounder (lrs) experiment on-board the selene spacecraft. *Earth, Planets and Space* **52**(9), 629–637 (2000). <https://doi.org/10.1186/bf03351671>
- [3] Bussey, D.B.J., Spudis, P.D., Mini-Rf Team: New Insights into Lunar Processes and History from Global Mapping by Mini-RF Radar. In: 42nd Annual Lunar and Planetary Science Conference. Lunar and Planetary Science Conference, p. 2086 (2011)
- [4] Lu, W., Li, Y., Ji, Y., Tang, C., Zhou, B., Fang, G.: Ultra-wideband mimo array for penetrating lunar regolith structures on the chang’e-5 lander. *Electronics* **10**(1), 8 (2020). <https://doi.org/10.3390/electronics10010008>
- [5] Seu, R., Phillips, R.J., Biccari, D., Orosei, R., Masdea, A., Picardi, G., Safaenili, A., Campbell, B.A., Plaut, J.J., Marinangeli, L., Smrekar, S.E., Nunes, D.C.: Sharad sounding radar on the mars reconnaissance orbiter. *Journal of Geophysical Research* **112**(E5) (2007). <https://doi.org/10.1029/2006je002745>
- [6] Orosei, R., Jordan, R.L., Morgan, D.D., Cartacci, M., Cicchetti, A., Duru, F., Gurnett, D.A., Heggy, E., Kirchner, D.L., Noschese, R., Kofman, W., Masdea, A., Plaut, J.J., Seu, R., Watters, T.R., Picardi, G.: Mars advanced radar for subsurface and ionospheric sounding (marsis) after nine years of operation: A summary. *Planetary and Space Science* **112**, 98–114 (2015). <https://doi.org/10.1016/j.pss.2014.07.010>
- [7] Hamran, S.-E., Paige, D.A., Amundsen, H.E.F., Berger, T., Brovoll, S., Carter, L., Damsgård, L., Dypvik, H., Eide, J., Eide, S., Ghent, R., Hellenen, O., Kohler, J., Mellon, M., Nunes, D.C., Plettemeier, D., Rowe, K., Russell, P., Øyan, M.J.: Radar imager for mars’ subsurface experiment—rimfax. *Space Science Reviews* **216**(8) (2020). <https://doi.org/10.1007/s11214-020-00740-4>
- [8] Moussessian, A., Blankenship, D.D., Plaut, J.J., Patterson, G.W., Gim, Y., Schroeder, D.M., Soderlund, K.M., Grima, C., Young, D.A., Chapin, E.: REASON for Europa. In: AGU Fall Meeting Abstracts, vol. 2015, pp. 13–05 (2015)
- [9] Grasset, O., Dougherty, M.K., Coustenis, A., Bunce, E.J., Erd, C., Titov, D., Blanc, M., Coates, A., Drossart, P., Fletcher, L.N., Hussmann, H., Jaumann, R., Krupp, N., Lebreton, J.-P., Prieto-Ballesteros, O., Tortora, P., Tosi, F., Van Hoolst, T.: JUPiter ICy moons Explorer (JUICE): An ESA mission to orbit Ganymede and to characterise the Jupiter system. *Planetary Space Science* **78**, 1–21 (2013). <https://doi.org/10.1016/j.pss.2012.12.002>
- [10] Kofman, W., Herique, A., Goutail, J.-P., Hagfors, T., Williams, I.P., Nielsen, E., Barriot, J.-P., Barbin, Y., Elachi, C., Edenhofer, P., Lvasseur-Regourd, A.-C., Plettemeier, D., Picardi, G., Seu, R., Svedhem,

- V.: The comet nucleus sounding experiment by radiowave transmission (consert): A short description of the instrument and of the commissioning stages. *Space Science Reviews* **128**(1-4), 413–432 (2007). <https://doi.org/10.1007/s11214-006-9034-9>
- [11] Ciarletti, V.: A variety of radars designed to explore the hidden structures and properties of the solar system’s planets and bodies. *Comptes Rendus Physique* **17**(9), 966–975 (2016). <https://doi.org/10.1016/j.crhy.2016.07.022>
- [12] Knight, R.: Ground penetrating radar for environmental applications. *Annual Review of Earth and Planetary Sciences* **29**(1), 229–255 (2001). <https://doi.org/10.1146/annurev.earth.29.1.229>
- [13] Tosti, F., Pajewski, L.: Applications of radar systems in planetary sciences: An overview. *Springer Transactions in Civil and Environmental Engineering*, 361–371 (2015). https://doi.org/10.1007/978-3-319-04813-0_15
- [14] Costello, E.S., Ghent, R.R., Lucey, P.G.: Secondary impact burial and excavation gardening on the moon and the depth to ice in permanent shadow. *Journal of Geophysical Research: Planets* **126**(9) (2021). <https://doi.org/10.1029/2021je006933>
- [15] Zyla, P.A., *et al.*: Review of Particle Physics. *PTEP* **2020**(8), 083–01 (2020). <https://doi.org/10.1093/ptep/ptaa104>
- [16] Hoover, S., Nam, J., Gorham, P.W., Grashorn, E., Allison, P., Barwick, S.W., Beatty, J.J., Belov, K., Besson, D.Z., Binns, W.R., Chen, C., Chen, P., Clem, J.M., Connolly, A., Dowkontt, P.F., Duvernois, M.A., Field, R.C., Goldstein, D., Viereg, A.G., Hast, C., Israel, M.H., Javaid, A., Kowalski, J., Learned, J.G., Liewer, K.M., Link, J.T., Lusczek, E., Matsuno, S., Mercurio, B.C., Miki, C., Miočinović, P., Naudet, C.J., Ng, J., Nichol, R.J., Palladino, K., Reil, K., Romero-Wolf, A., Rosen, M., Ruckman, L., Saltzberg, D., Seckel, D., Varner, G.S., Walz, D., Wu, F.: Observation of Ultrahigh-Energy Cosmic Rays with the ANITA Balloon-Borne Radio Interferometer. *Physical Review Letters* **105**(15), 151101 (2010) [arXiv:1005.0035](https://arxiv.org/abs/1005.0035) [astro-ph.HE]. <https://doi.org/10.1103/PhysRevLett.105.151101>
- [17] Aab, A., Abreu, P., Aglietta, M., Samarai, I.A., Albuquerque, I.F.M., Allekotte, I., Almela, A., Castillo, J.A., Alvarez-Muñiz, J., Anastasi, G.A., *et al.*: Combined fit of spectrum and composition data as measured by the pierre auger observatory. *Journal of Cosmology and Astroparticle Physics* **2017**(04), 038–038 (2017). <https://doi.org/10.1088/1475-7516/2017/04/038>
- [18] Rémy, F., Parouty, S.: Antarctic ice sheet and radar altimetry: A review. *Remote Sensing* **1**(4), 1212–1239 (2009). <https://doi.org/10.3390/rs1041212>
- [19] Verzi, V., Ivanov, D., Tsunesada, Y.: Measurement of energy spectrum of ultra-high energy cosmic rays. *Progress of Theoretical and Experimental Physics* **2017**(12) (2017). <https://doi.org/10.1093/ptep/ptx082>

- [20] Tueros, M., Sciutto, S.J.: Tierras: A package to simulate high energy cosmic ray showers underground, underwater and under-ice. *Comput. Phys. Commun.* **181**, 380–392 (2010)
- [21] Alvarez-Muñiz, J., Carvalho, W.R., Zas, E.: Monte Carlo simulations of radio pulses in atmospheric showers using ZHAireS. *Astroparticle Physics* **35**(6), 325–341 (2012) [arXiv:1107.1189](https://arxiv.org/abs/1107.1189) [astro-ph.HE]. <https://doi.org/10.1016/j.astropartphys.2011.10.005>
- [22] Askar’yan, G.A.: Excess negative charge of an electron-photon shower and its coherent radio emission. *Zh. Eksp. Teor. Fiz.* **41**, 616–618 (1961)
- [23] Cherenkov, P.A.: Visible emission of clean liquids by action of γ radiation. *Doklady Akademii Nauk SSSR* **451** (1934)
- [24] Tamm, I.E.: General characteristics of vavilov-cherenkov radiation. *Science* **131**(3395), 206–210 (1960). <https://doi.org/10.1126/science.131.3395.206>
- [25] Saltzberg, D., Gorham, P., Walz, D., Field, C., Iverson, R., Odian, A., Resch, G., Schoessow, P., Williams, D.: Observation of the Askaryan effect: Coherent microwave Cherenkov emission from charge asymmetry in high-energy particle cascades. *Phys. Rev. Lett.* **86**, 2802–2805 (2001) [arXiv:hep-ex/0011001](https://arxiv.org/abs/hep-ex/0011001). <https://doi.org/10.1103/PhysRevLett.86.2802>
- [26] Gorham, P.W., Saltzberg, D., Field, R.C., Guillian, E., Milincic, R., Walz, D., Williams, D.: Accelerator measurements of the Askaryan effect in rock salt: A Roadmap toward teraton underground neutrino detectors. *Phys. Rev. D* **72**, 023002 (2005) [arXiv:astro-ph/0412128](https://arxiv.org/abs/astro-ph/0412128). <https://doi.org/10.1103/PhysRevD.72.023002>
- [27] Gorham, P.W., *et al.*: Observations of the Askaryan effect in ice. *Phys. Rev. Lett.* **99**, 171101 (2007) [arXiv:hep-ex/0611008](https://arxiv.org/abs/hep-ex/0611008). <https://doi.org/10.1103/PhysRevLett.99.171101>
- [28] Gorham, P.W., *et al.*: Picosecond timing of Microwave Cherenkov Impulses from High-Energy Particle Showers Using Dielectric-loaded Waveguides. *Phys. Rev. Accel. Beams* **21**(7), 072901 (2018) [arXiv:1708.01798](https://arxiv.org/abs/1708.01798) [physics.ins-det]. <https://doi.org/10.1103/PhysRevAccelBeams.21.072901>
- [29] Allison, P., Auffenberg, J., Bard, R., Beatty, J.J., Besson, D.Z., Boeser, S., Chen, C., Chen, P., Connolly, A., Davies, J., DuVernois, M., Fox, B., Gorham, P.W., Grashorn, E.W., Hanson, K., Haugen, J., Helbing, K., Hill, B., Hoffman, K.D., Huang, M., Huang, M.H.A., Ishihara, A., Karle, A., Kennedy, D., Landsman, H., Landrie, A., Liu, T.C., Macchiarulo, L., Mase, K., Meures, T., Meyhandan, R., Miki, C., Morse, R., Newcomb, M., Nichol, R.J., Ratzlaff, K., Richman, M., Ritter, L., Rotter, B., Sandstrom, P., Seckel, D., Touart, J., Varner, G.S., Wang, M.-Z., Weaver, C., Wendorff, A., Yoshida, S., Young, R.: Design and initial performance of the askaryan radio array prototype eev neutrino detector at the south pole (2011) [arXiv:1105.2854v2](https://arxiv.org/abs/1105.2854v2). <https://doi.org/10.1016/j.icarus.2012.05.028>
- [30] Anker, A., Barwick, S.W., Bernhoff, H., Besson, D.Z., Bingefors, N., Gaswint, G., Glaser, C., Hallgren, A., Hanson, J.C., Lahmann, R., Latif,

- U., Nam, J., Novikov, A., Klein, S.R., Kleinfelder, S.A., Nelles, A., Paul, M.P., Persichilli, C., Shively, S.R., Tatar, J., Unger, E., Wang, S.-H., Yodh, G.: Targeting ultra-high energy neutrinos with the arianna experiment. *Advances in Space Research* 64 (2019) 2595-2609 (2019) [arXiv:1903.01609v2](https://arxiv.org/abs/1903.01609v2). <https://doi.org/10.1016/j.asr.2019.06.016>
- [31] Gorham, P.W.: The ANITA cosmogenic neutrino experiment. *Acoustic and Radio EeV Neutrino Detection Activities* (2006). https://doi.org/10.1142/9789812773791_0029
- [32] Alvarez-Muñiz, J., Romero-Wolf, A., Zas, E.: Practical and accurate calculations of askaryan radiation. *Phys. Rev. D* 84, 103003 (2011) (2011) [arXiv:1106.6283v3](https://arxiv.org/abs/1106.6283v3). <https://doi.org/10.1103/PhysRevD.84.103003>
- [33] Yee, K.: Numerical solution of initial boundary value problems involving maxwell's equations in isotropic media. *IEEE Transactions on Antennas and Propagation* 14(3), 302–307 (1966). <https://doi.org/10.1109/TAP.1966.1138693>
- [34] Remcom Incorporated: XFDTD. <https://www.remcom.com/xfdtd-3d-em-simulation-software>
- [35] Fang, G.-Y., Zhou, B., Ji, Y.-C., Zhang, Q.-Y., Shen, S.-X., Li, Y.-X., Guan, H.-F., Tang, C.-J., Gao, Y.-Z., Lu, W., Ye, S.-B., Han, H.-D., Zheng, J., Wang, S.-Z.: Lunar penetrating radar onboard the chang'e-3 mission. *Research in Astronomy and Astrophysics* 14(12), 1607–1622 (2014). <https://doi.org/10.1088/1674-4527/14/12/009>
- [36] Yuan, Y., Zhu, P., Zhao, N., Xiao, L., Garnero, E., Xiao, Z., Zhao, J., Qiao, L.: The 3-d geological model around chang'e-3 landing site based on lunar penetrating radar channel 1 data. *Geophysical Research Letters* 44(13), 6553–6561 (2017). <https://doi.org/10.1002/2017gl073589>
- [37] Shepard, M.K., Brackett, R.A., Arvidson, R.E.: Self-affine (fractal) topography: Surface parameterization and radar scattering. *Journal of Geophysical Research* 100(E6), 11709–11718 (1995). <https://doi.org/10.1029/95JE00664>
- [38] Aab, A., Abreu, P., Aglietta, M., Samarai, I.A., Albuquerque, I.F.M., Allekotte, I., Almela, A., Castillo, J.A., Alvarez-Muñiz, J., Anastasi, G.A., et al.: Combined fit of spectrum and composition data as measured by the pierre auger observatory. *Journal of Cosmology and Astroparticle Physics* 2017(04), 038–038 (2017). <https://doi.org/10.1088/1475-7516/2017/04/038>
- [39] Viereg, A.G., Bechtol, K., Romero-Wolf, A.: A technique for detection of pev neutrinos using a phased radio array. *JCAP* 2 (2016) 005 (2015) [arXiv:1504.08006v2](https://arxiv.org/abs/1504.08006v2). <https://doi.org/10.1088/1475-7516/2016/02/005>